Available online at www.sciencedirect.com
SCIENCE DIRECT®
Infrared Physics & Technology 44 (2003) 337–346
INFRARED PHYSICS & TECHNOLOGY
www.elsevier.com/locate/infrared

Electron transfer based voltage tunable two-color quantum-well infrared photodetectors

Amlan Majumdar [a,*], K.K. Choi [b,*], J.L. Reno [c], L.P. Rokhinson [a], D.C. Tsui [a]

[a] Department of Electrical Engineering, Princeton University, Princeton, NJ 08544, USA
[b] Electro-optics and Photonics Division, US Army Research Laboratory, 2800 Powder Mill Road, Adelphi, MD 20783, USA
[c] Sandia National Laboratories, Albuquerque, NM 87185, USA

Abstract

We present a detailed investigation of the temperature T dependence of photoresponse of voltage tunable two-color quantum-well infrared photodetectors (QWIPs) that are based on the transfer of electrons between coupled QWs under an applied bias V_b. For $T \leqslant 40$ K, the peak detection wavelength switches from 7.2 μm under positive bias to 8.6 μm under large negative bias as electrons are transferred from the right QW (RQW) to the left QW (LQW). For $T \geqslant 50$ K, the short wavelength peak is not only present for both bias polarities but also increases rapidly with T while the long wavelength peak decreases rapidly with T. We investigate this temperature dependence by extracting absorption coefficient α and photoconductive gain g using corrugated QWIPs with different corrugation periods. The deduced absorption spectra indicate that the LQW population first increases and then decreases with increasing negative bias for $T \geqslant 50$ K. The deduced gain spectra show that short and long wavelength gain under negative bias exhibit a strong enhancement and reduction, respectively, with T above 50 K. We show that both these temperature dependences are caused by large thermal currents from the LQWs, which are designed for long wavelength detection and, therefore, have a significantly lower activation energy than the RQWs.

PACS: 78.30.Fs; 78.67.De

Keywords: Quantum-well infrared photodetectors; Two-color; Voltage tunable detectors; Coupled quantum wells

1. Introduction

The fabrication of two-color quantum-well infrared photodetectors (QWIPs) has been an area of intense research for the past decade as these detectors have a lot of important applications, such as, remote temperature sensing and chemical analysis [1,2]. Two-stack detector [3,4], which are the simplest two-color detectors, are three-terminal devices that lead to complicated readout electronics [5,6]. Voltage tunable detectors, which are two-terminal devices, when integrated with time-multiplexed readout circuits immensely simplify focal plane array production. Voltage tunable detectors that have been demonstrated in the past were based on either Stark-shift [7–10] or multiple

* Corresponding authors. Tel.: +1-609-258-5606; fax: +1-609-258-1840 (A. Majumdar), tel.: +1-301-394-0495; fax: +1-301-394-5451 (K.K. Choi).
E-mail addresses: majumdar@ee.princeton.edu (A. Majumdar), kchoi@arl.army.mil (K.K. Choi).

1350-4495/$ - see front matter
doi:10.1016/S1350-4495(03)00153-1

transitions in heavily-doped QWs [11,12]. Both these methods have certain drawbacks, such as, small tuning range for Stark-shift based detectors and very low detectivities for multiple-transition based detectors.

Another mechanism that can be utilized for voltage tunable detection is the transfer of electrons between coupled QWs under an applied bias [13]. The left QWs (LQWs) and the right QWs (RQWs) in these multiple QW (MQW) structures are designed to detect different wavelengths. The peak detection wavelength of these two-color detectors should shift from one wavelength to the other as the polarity of the applied bias is reversed. While this electron transfer mechanism was used for demonstrating infrared modulators [14–16], past attempts at fabricating voltage tunable two-color detectors were unsuccessful because the shorter wavelength peak was present for both bias polarities V_b [17]. Recently, we identified and then rectified problems with the design of these detectors [18,19]. Subsequently, we demonstrated a two-color detector where the peak detection wavelength λ_p shifts from 7.5 to 8.8 μm as the bias polarity is reversed at temperature $T = 10$ K for $|V_b| \geqslant 3$ V [20].

In this article, we present a detailed investigation of the temperature dependence of photoresponse of electron transfer based voltage tunable detectors that exhibit complete wavelength switching from $\lambda_p = 7.2$ to 8.6 μm for $|V_b| \geqslant 3$ V for $T \leqslant 40$ K. At higher temperatures, the short wavelength peak is not only present for both bias polarities but also becomes the primary detection peak for both bias polarities. We investigate this temperature dependence by extracting absorption coefficient α and photoconductive gain g using corrugated QWIPs (CQWIPs) with different corrugation periods [21–23]. The deduced absorption and gain spectra indicate that the origin of the high temperature behavior can be traced back to large thermal currents from the LQWs, which are designed for long wavelength detection and, therefore, have a smaller activation energy than the RQWs.

This article is organized as follows. We describe the detector structure in Section 2, show responsivity data in Section 3, and extract α and g in Section 4. We present the deduced absorption and gain spectra in Sections 5 and 6, respectively, and analyze their temperature dependence. Finally, we present our conclusions in Section 7.

2. Detector structure

The detector structure consists of 36 periods of QW pairs that are sandwiched between two n^+-GaAs contact layers. Each period of the MQW structure has a 44 Å $Al_{0.05}Ga_{0.95}As$ LQW coupled to a 44 Å GaAs RQW through a 200 Å $Al_{0.3}Ga_{0.7}As$ barrier and separated from the next set of QW pair by a 350 Å graded $Al_xGa_{1-x}As$ barrier ($x = 0.3 \rightarrow 0.25$ along the growth direction). The LQWs are uniformly doped with a Si donor density of $N_D = 1.2 \times 10^{18}$ cm^{-3}. The RQWs and the barriers are undoped. The entire

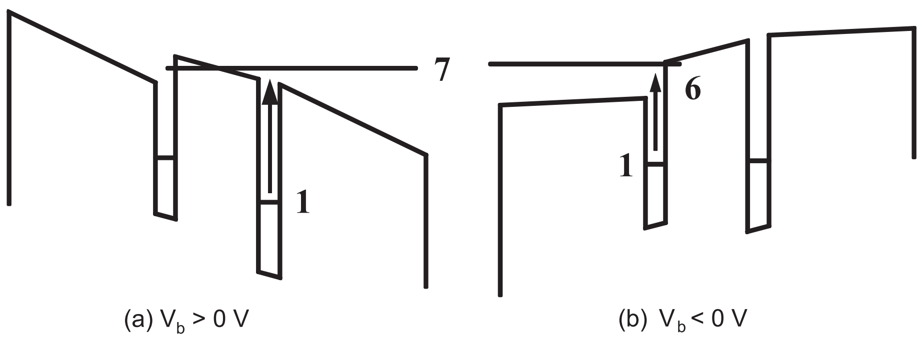

Fig. 1. Conduction band diagram of coupled QWs for voltage tunable two-color detection under (a) positive and (b) negative bias V_b. The arrows indicate transitions, $E_1 \rightarrow E_7$ (R7) at $V_b = 3$ V and $E_1 \rightarrow E_6$ (L6) at $V_b = -3$ V, that have the largest calculated oscillator strength.

structure was grown on a semi-insulating (1 0 0)-GaAs substrate by molecular beam epitaxy.

The conduction band diagram of the coupled QWs is sketched in Fig. 1. V_b is applied to the top contact while the bottom one is kept grounded. For positive bias and small negative bias, the lowest energy level E_1 is in the RQW and moves to the LQW at large negative bias. The maximum value of calculated oscillator strength f at $V_b = 3$ V occurs at 7.6 μm, which corresponds to the $E_1 \rightarrow E_7$ transition as indicated in Fig. 1. We call this transition R7 because E_1 is in the RQW. At $V_b = -3$ V, the $E_1 \rightarrow E_6$ (L6) transition at $\lambda_{L6} = 10.1$ μm has the largest oscillator strength. Other significant transitions are L7 at $\lambda_{L7} = 8.9$ μm and L8 at $\lambda_{L8} = 8.3$ μm with $f = 65\%$ and 20% of f_{L6}, respectively. All these transitions are bound-to-continuum transitions and, therefore, should have large photoconductive gain.

3. Responsivity

We processed 45°-edge coupled detectors for basic detector characterization. Spectral responsivity of these detectors was measured in the 10–70 K temperature range using standard ac lock-in techniques. We show typical responsivity spectra at $T = 10$, 50, and 70 K in Fig. 2. Under positive bias, the detector has a narrow detection peak whose position $\lambda_p = 7.2$ μm and line width $\Delta\lambda = 0.6$ μm, defined as the full width at half-maxima, do not depend on V_b and T. The cutoff wavelength is $\lambda_c = 7.5$ μm. The peak responsivity $R(\lambda_p)$ increases with V_b but is independent of T. Under negative bias at $T = 10$ K, there is a wide responsivity peak at 7.2 μm at $V_b = -1.5$ V. With increasing $|V_b|$, a broad peak appears at 8.6 μm while the size of the short wavelength peak decreases as electrons are transferred from the RQW to the LQW. For $V_b \leqslant -3$ V, there is complete switching of the detection peak to $\lambda_p = 8.6$ μm with line width $\Delta\lambda = 4.1$ μm. Switching the bias polarity for $|V_b| \geqslant 3$ V leads to a 1.4 μm shift in λ_p and a 3.5 μm change in λ_c, which clearly demonstrates the voltage tunability of this detector. As the detector temperature is raised above $T = 10$ K, the negative bias responsivity spectra do not change up to $T = 40$ K. At higher temperatures, a short wavelength peak at 7.2 μm is present for negative voltages. The long wavelength peak decreases in size and shifts to 9 μm for $|V_b| < 3$ V at $T = 50$ K. At an even higher temperature $T = 70$ K, the detection peak is narrow and centered around 7.2 μm for both the detectors.

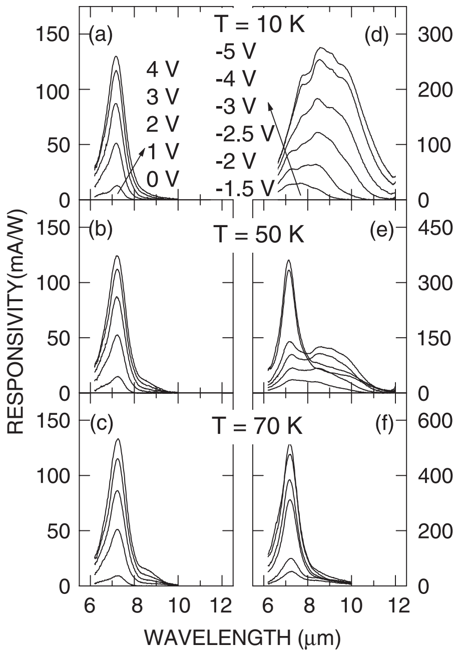

Fig. 2. Responsivity of 45°-edge coupled detectors at (a,d) $T = 10$ K; (b,e) $T = 50$ K; and (c,f) $T = 70$ K.

We note that this detector has a short-circuit photocurrent at zero bias peaked at the shorter detection wavelength. This photovoltaic behavior arises from the presence of a built-in electric field in the graded barrier regions [8,10,24]. As mentioned earlier, the LQW is not populated at zero bias, which explains the absence of the photovoltaic effect in the long wavelength range.

4. Extraction of detector parameters

The presence of the short wavelength peak in detector response for negative bias voltages and its significant enhancement with increasing temperature for $T \geqslant 40$ K is quite surprising. We investigate these observations by extracting absorption coefficient α and photoconductive gain g at different temperatures using a set of eight CQWIPs with corrugation period $P = 10, 15, 20, 30, 40, 60, 300$, and 1200 μm [21–23]. We measured spectral responsivity of the CQWIPs at $T = 10$, 50, and 70 K. The responsivity line shape of all the CQWIPs is similar to that of the 45°-edge coupled detectors and, therefore, are not shown here.

We convert responsivity R to normalized responsivity NR using $\mathrm{NR}(P) = R(P)/r_d(P)$, where $r_d(P) = I_d(P)/I_d$ ($P = 1200$ μm) is the dark current ratio measured at $T = 77$ K [23]. Using NR instead of R for the data fitting procedure discussed below allows us to compensate for material variations that arise from processing non-uniformities. Typical NR spectra of CQWIPs are shown in Fig. 3(a) for $V_b = 3$ V and $T = 10$ K. We obtain the values of NR at fixed wavelengths for different values of P from Fig. 3(a) and plot them as a function of P in Fig. 3(b) and (c). We fit the following equation to the NR vs. P data [23]:

$$\mathrm{NR}(P) = \frac{e}{h\nu} g \frac{1}{P-t}\left(t + \frac{e^{-\alpha P}}{2\alpha}(1 - e^{2\alpha t})\right) + R_0 \frac{P}{P-t}, \quad (1)$$

where $h\nu$ is the energy of incident radiation and $t = 2.8$ μm is the CQWIP etch depth. R_0 is the CQWIP responsivity when P is very large and attributed to responsivity from p-polarized light reflected by the two mesa edges that are perpendicular to the corrugations [25]. α, g, and R_0 are all assumed to be material constants and used as fitting parameters. The least-squares fits, plotted in Fig. 3(b) and (c), indicate that Eq. (1) fits the data well. We repeat this fitting process for all values of V_b and T. The deduced spectra of R_0 are not shown here as they do not throw much light on the temperature dependence of detector responsivity. The deduced spectra of α and g are presented in the next two sections.

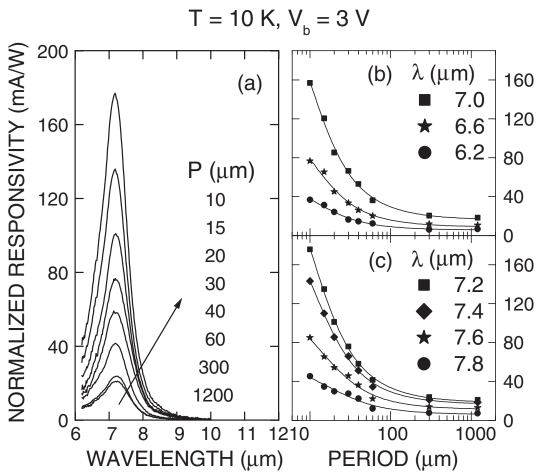

Fig. 3. Normalized responsivity 'NR' of CQWIPs with different corrugation period P. (a) NR spectra at $V_b = 3$ V and $T = 10$ K. (b,c) NR vs. P at different wavelengths λ. Symbols: data; Lines: least-squares fit of Eq. (1) to the data.

5. Absorption coefficient

5.1. Deduced spectra

The deduced values of absorption coefficient α are plotted as circles in Fig. 4. Under positive bias in the 10–70 K temperature range, there is an absorption peak around 7 μm. This peak is assigned to the R7 transition ($\lambda_{R7} = 7.6$ μm for nominal structure parameters) in the RQW, which is the only occupied well under positive bias. Under negative bias up to −2 V at $T = 10$ K, there are two absorption peaks at 7 and 8.3 μm that correspond to the R7 and L8 transitions, respectively. At higher negative voltages, the 7 μm peak disappears while the 8.3 μm peak gets significantly broader. The broadening of the 8.3 μm peak could be due to the closely spaced L7 transition at $\lambda_{L7} = 8.9$ μm that is not resolved separately. A third peak around 10.8 μm, which could be a shifted L6 transition, appears at $V_b = -2.5$ V and becomes the main peak beyond $V_b = -4$ V. At $T = 50$ K, there are absorption peaks at 7, 8.5, and 10.2 μm that are attributed to the R7, combined L7 and L8, and L6 transitions, respectively. The peak at 8.5 μm is the main peak at all negative voltages. At $T = 70$ K, the absorption peak shifts from 8.6 μm, the combined L7 and L8 transitions, to 7 μm, the R7 transition, at $V_b = -2.5$ V with the 8.6 μm peak disappearing beyond $V_b = -4$ V.

The relative size of the absorption peaks should reflect the ratio of the oscillator strengths f. This is, however, not the case under negative bias as the calculated values of f_{L7} and f_{L8} are 65% and 20%

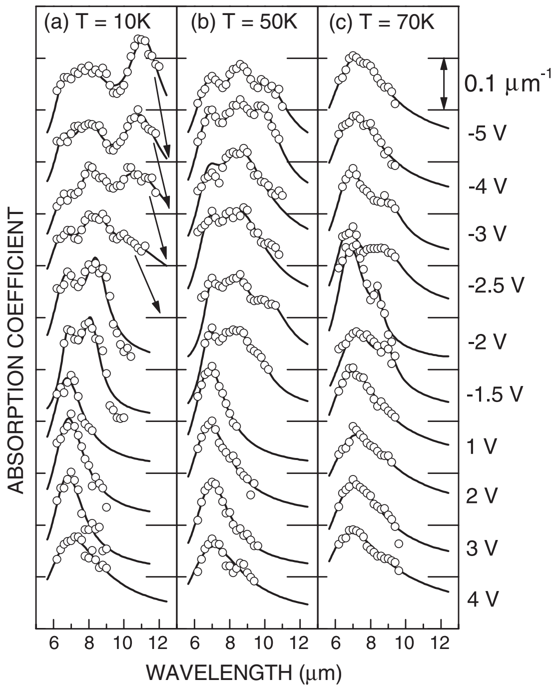

Fig. 4. Spectrum of absorption coefficient α in the 10–70 K temperature range. Each curve has been shifted by 0.1 μm^{-1} from the one just below it for clarity. The arrows indicate the baseline ($\alpha = 0$) for cases where the baseline is not clear. The bias voltages V_b are indicated on the right margin. Symbols: α obtained from fitting Eq. (1) to normalized responsivity data. Lines: least-squares fit of single or multiple Lorentzians to α. Typical error bars of 10% are not shown for clarity.

of f_{L6}, respectively. Since Stark shifts are small in this structure, the small discrepancies in the locations and magnitudes between the observed transitions and the calculated ones at $V_b = \pm 3$ V are attributed to differences in the nominal and actual detector structures. These differences, however, do not affect the following data analysis.

5.2. Quantum well electron densities

We now look into the electron transfer process in greater detail to understand the temperature dependence of the absorption peaks. We evaluate the integrated absorption strength (IAS) of the observed transitions and then use them to determine the LQW and RQW electron densities, n_L and n_R, respectively. This is possible because the IAS of an intersubband transition is $A_T \propto f_T n_{2D}/m^*$, where f_T is the oscillator strength, n_{2D} the two-dimensional (2D) electron density in the QW, and m^* the electronic effective mass [1]. The IAS of the individual transitions is obtained by fitting Lorentzians of the form $\alpha(E) = A_T \Delta E / (2\pi[(E - E_p)^2 + (\Delta E/2)^2])$ to the absorption data. Here E is energy and A_T, E_p and ΔE, which are fitting parameters, are the IAS, peak position and full width at half maxima, respectively. We use one Lorentzian under positive bias and two or three Lorentzians under negative bias to match the number of peaks found in the absorption data. The least-squares fit are shown in Fig. 4 with lines. Note that we use the peak positions E_p as fitting parameters also because the observed peak energies are different from the ones calculated at $V_b = 3$ and -3 V.

After obtaining the values of A_T for different transitions from the fitting procedure, n_L and n_R are obtained by the following method. The IAS of the R7 transition in the RQW is $A_{R7} \propto f_{R7} n_R / m_R^*$, where f_{R7} is the oscillator strength of the R7 transition and m_R^* is the effective mass of electrons in the RQW. f_{R7} is insensitive to the magnitude and polarity of V_b because both the initial state and final states of the R7 transition are localized in the RQW. Under negative bias, the final state wave functions of the LQW transitions are more delocalized throughout the MQW periods, and thus, the individual oscillator strengths can change with V_b. However, due to the oscillator strength sum rule [1], the total f of all the prominent LQW transitions will remain almost unchanged with V_b. Therefore, the sum of the IAS of the long wavelength transitions in the LQW is $A_L \propto f_L n_L / m_L^*$, where f_L is the bias-insensitive sum of oscillator strengths of the observed long wavelength transitions and m_L^* is the effective mass of electrons in the LQW. Using the above two expressions for A_{R7} and A_L with $n_{2D} = n_L + n_R$, where n_{2D} is the total 2D electron density in each period of the MQW structure, we obtain $n_L = n_{2D}/(1 + (m_R^* f_L A_{R7} / m_L^* f_{R7} A_L))$ and $n_R = n_{2D}/(1 + (m_L^* f_{R7} A_L / m_R^* f_L A_{R7}))$. We use the values of A_{R7} and A_L determined from the fitting procedure, the calculated ratio f_L/f_{R7} at $|V_b| = 3$ V, $m_L^* = 0.0707 m_0$, and $m_R^* = 0.0665 m_0$, where m_0 is the free-electron mass, to determine n_L and n_R. These densities at $T = 10$,

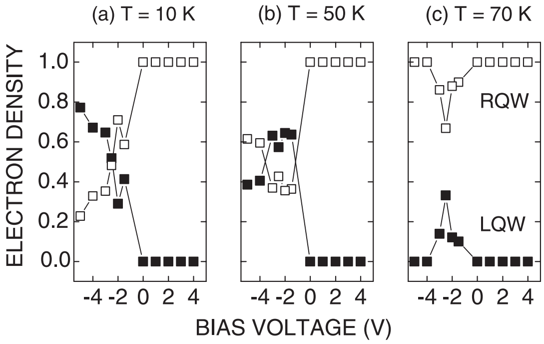

Fig. 5. 2D electron density in the LQW (n_L/n_{2D}) and the RQW (n_R/n_{2D}) at temperature: (a) $T = 10$ K, (b) $T = 50$ K, and (c) $T = 70$ K. The total 2D electron density $n_{2D} = 5.3 \times 10^{11}$ cm^{-2}.

50, and 70 K are plotted in Fig. 5, which brings out the following trends: (i) all electrons are in the RQW under positive bias and are transferred to the LQW at $T = 10$ K as a negative bias is applied across the detector, and (ii) at higher temperatures, n_L increases with $|V_b|$ at low negative bias and decreases with $|V_b|$ at high negative bias. This depletion of the LQW increases dramatically with temperature above $T = 50$ K. The first trend result from the equalization of the Fermi level between the LQW and the RQW in each MQW period. The second one is, however, unexpected and cannot be explained by the above argument.

At high temperatures, a large number of electrons escape from QWs via thermionic emission. The number of these thermally generated electrons is $n_{th} \propto \exp(-(E_b - E_F)/k_BT) = \exp(-(E_b - E_1)/k_BT)[\exp(n_{QW}/g_{2D}k_BT) - 1]$, where E_F is the Fermi energy, E_1 the ground state energy, n_{QW} the 2D electron density in the QW, and g_{2D} the 2D density of states [1,26,27]. Therefore, the number of thermal electrons that escape from the LQW and the RQW are given by $n_{Lth} \propto \exp(-(E_{bL} - E_{1L})/k_BT)[\exp(n_L/g_{2D}k_BT) - 1]$ and $n_{Rth} \propto \exp(-(E_{bR} - E_{1R})/k_BT)[\exp(n_R/g_{2D}k_BT) - 1]$, respectively, where E_{bL} is the height of the graded barrier seen by the LQW electrons under negative bias, E_{bR} the height of the middle barrier seen by the RQW electrons under negative bias, E_{1L} the LQW ground state energy, and E_{1R} the RQW ground state energy. For the nominal material parameters, $E_{bL} - E_{1L}$ is significantly smaller than $E_{bR} - E_{1R}$. Activation energy, deduced from the temperature dependence of detector dark current, is appreciably lower under negative bias than under positive bias [20]. Therefore, we have experimentally confirmed that $E_{bL} - E_{1L} \gg E_{bR} - E_{1R}$. The continuity of dark current implies that $n_{Lth} = n_{Rth}$. Since $E_{bL} - E_{1L} \ll E_{bR} - E_{1R}$, it is clear from the equality of the above two expressions for n_{Lth} and n_{Rth} that $n_L \ll n_R$. Therefore, the depletion of the LQW at high negative bias and high temperature can be explained by the continuity of dark current due to the thermal electrons that have significantly lower activation energy in the LQW.

6. Photoconductive gain

6.1. Deduced spectra

The deduced values of photoconductive gain g are shown in Fig. 6. Under positive bias, the gain spectra have a peak at 7.2 μm which exhibits negligible temperature dependence in the 10–70 K range. Also, gain is small below 6 μm and above 8 μm. The lower cutoff wavelength λ_L is set by the position of the L-valleys in the barriers as scattering from the Γ- to the L-valleys lowers the photoelectron mobility. The L-valleys in $Al_xGa_{1-x}As$ ($x \approx 0.3$) are $\Delta E_L \approx 310$ meV above the GaAs band edge. Therefore, $\lambda_L = hc/(\Delta E_L - E_{1R}) = 5.5$ μm. The upper cutoff wavelength λ_U is determined by the barrier height E_B as photoelectrons with energy less than E_B are trapped in the QW and, hence, have low gain. $E_B = 225$ meV for the $Al_{0.3}Ga_{0.7}As$ barrier yields $\lambda_U = hc/(E_B - E_{1R}) = 8.5$ μm. These calculated values of λ_L and λ_U are in satisfactory agreement with $\lambda_L \approx 6$ μm and $\lambda_U \approx 8.5$ μm found in Fig. 6.

Under negative bias at $T = 10$ K, the gain peak switches from 7.2 μm at $V_b = -1.5$ V to 8.6 μm at $V_b = -3$ V with peaks at both 7.2 and 8.6 μm for intermediate bias voltages. Under negative bias, the expected lower cutoff wavelength, set by the position of the L-valleys in the barriers, is $\lambda_L = hc/(\Delta E_L - E_{1L}) = 5.2$ μm, which is consistent with $\lambda_L \approx 6$ μm in Fig. 6. The upper cutoff wavelength, determined by the barrier height, is expected to change with V_b because the barrier height is set by the left edge of the graded barrier

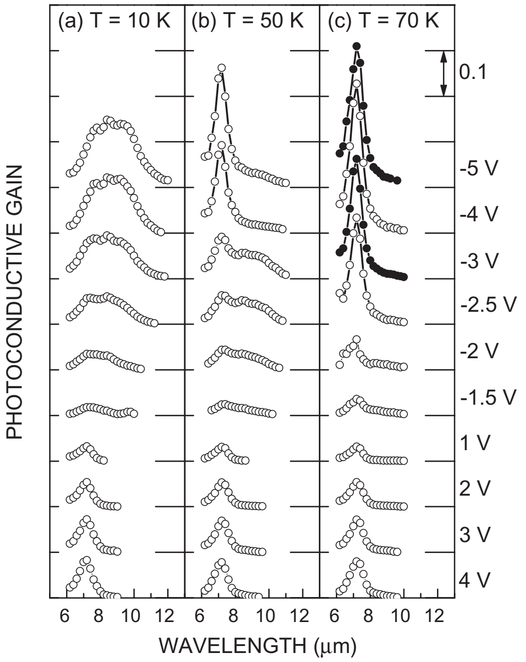

Fig. 6. Photoconductive gain g spectra in the 10–70 K temperature range. The bias voltages V_b are indicated on the right margin. g is obtained from fitting Eq. (1) to normalized responsivity data. Each curve has been shifted by 0.1 from the one just below it for clarity. Typical error bars of 10% are not shown for clarity.

($Al_{0.3}Ga_{0.7}As$ with $E_B = 225$ meV) at low negative V_b and by the right edge ($Al_{0.25}Ga_{0.75}As$ with $E_B = 187.5$ meV) at high negative V_b (Fig. 1). Therefore, we expect $\lambda_U = 8$ μm at low negative V_b and $\lambda_U = 11$ μm at high negative V_b. These values are in good agreement with data shown in Fig. 6 where λ_U increases from 9 to 11 μm as V_b is varied from −1.5 to −5 V.

As temperature is raised above $T = 10$ K, a short wavelength gain peak appears under negative bias at 7.2 μm, the same wavelength at which the positive bias gain has a peak at all temperatures. With increasing temperature, this 7.2 μm peak grows and eventually becomes the main peak. The peak size at $T = 50$ K and $V_b = -4$ V is 0.2. With further increase in temperature, the 7.2 μm peak becomes larger and sharper. At $T = 70$ K, the peak size at $V_b = -4$ V is 0.33. The enhancement of the short wavelength gain is accompanied by a reduction of the long wavelength gain. Also, the position of the long wavelength peak shifts to slightly larger wavelengths at higher temperatures. At $T = 50$ K, the long wavelength peak appears at 8.8 μm from $V_b = -2$ to −3 V. It is evident from the $T = 70$ K gain spectra that with further increase in temperature, the long wavelength peak completely disappears under negative bias. The peak values of gain are plotted in Fig. 7 as a function of V_b for different temperatures.

6.2. Discussion

In all our discussions so far, we have assumed that an applied bias leads to a constant electric field across each MQW period and is superimposed on the built-in electric field that exists at zero bias. This assumption is valid at low temperatures because the doped QWs are much thinner than the undoped barriers. A constant electric field leads to voltage division between the 200 Å middle barrier and the 350 Å graded barrier that is proportional to the width of the two barriers. This energy band picture (Fig. 1) can explain the following features of the gain data shown in Figs. 6 and 7.

Photoconductive gain is $g = v_d\tau/L$, where v_d is the photoelectron drift velocity, τ the photoelectron lifetime, and L the detector length. At low bias voltages, $v_d \propto F \propto V_b$, where F is the electric field in the barriers. Therefore, g should increase linearly with V_b, which is case for both short and long wavelength gain in the −3 to 3 V bias range at $T = 10$ K and for the short wavelength gain at $T = 50$ K, also in the −3 to 3 V bias range (Fig. 7). At higher bias voltages, the peak gain plotted in Fig. 7 shows signs of saturation. This is due to the scattering of photoelectrons from the Γ-valley to the L-valleys in the barrier region, which lowers the photoelectron mobility, and hence, photoconductive gain. Another important feature of the gain data shown in Fig. 7 is the negligible temperature dependence up to $T = 50$ K under low negative bias. This behavior is similar to that of one-color detectors, where both photoconductive and noise gains are found to be independent of temperature in the 10–80 K range, which suggests that the photoelectron mobility is temperature insensitive [23,28].

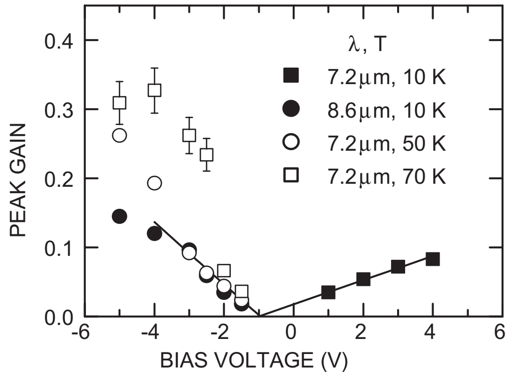

Fig. 7. Bias dependence of the short (7.2 μm) and long (8.6 μm) wavelength gain peak at $T = 10$, 50, and 70 K. Symbols: data from Fig. 6. Lines: linear fits in the low bias range.

The enhancement of the short wavelength gain peak at negative voltages above $T = 50$ K and the corresponding reduction of the long wavelength gain cannot be explained by the low temperature energy bands. At higher temperatures such as 70 K, it is possible for the graded barrier to have a lower resistance than the middle barrier despite its larger barrier width because the activation energy of the LQW is significantly smaller than that of the RQW. Therefore, a smaller part of the applied voltage would drop across the graded barrier, as depicted in Fig. 8. The conduction band diagram sketched in Fig. 8 is qualitatively consistent with the charge densities in the QWs shown in Fig. 5. Based on Gauss's Law, the band bending near the LQW implies that the LQW has a net positive charge while the band bending near the RQW implies that the RQW has a net negative charge. This is true at high temperatures under negative bias for the following reason. The LQW has a doping density of N_D donors while the RQW is undoped. At high temperatures and negative bias, the 2D electron density in the LQW n_L is significantly lower than $n_{2D} = L_w N_D$ as shown in Fig. 5. Therefore, the net 2D charge density in the LQW is $eL_wN_D + (-en_L) > 0$. On the other hand, the net 2D charge density in the RQW is $(-en_R) < 0$. Hence, the negative bias energy band diagram that is illustrated in Fig. 8 for high temperatures is qualitatively consistent with the doping profile and the QW electron densities that were determined from the absorption data.

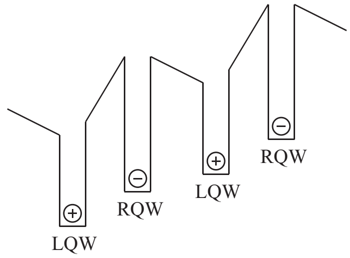

Fig. 8. Conduction band diagram of two-color detector under negative bias at high temperatures T. The energy bands are drawn under the assumption that all of the applied voltage drop per MQW period drops across the 200 Å middle barrier. The + and − signs indicate the polarity of the net charge in the LQWs and the RQWs, respectively.

It is clear from Fig. 8 that the excited state of the long wavelength photoelectrons, which are excited out of the LQW, is trapped in a V-shape potential well bound by the graded and middle barriers on two sides. This would significantly lower the gain of the long wavelength photoelectrons, which is consistent with the $T = 50$ and 70 K data shown in Figs. 6 and 7.

The electric field $F_{MB,HT}$ in the middle barrier at high temperatures is much higher than the field $F_{MB,LT}$ at low temperatures. If all of the applied voltage per MQW period dropped across the middle barrier at high temperatures, then $F_{MB,HT}/F_{MB,LT} = (L_{MB} + L_{GB})/L_{MB} = 2.75$, where $L_{MB} = 200$ Å is the thickness of the middle barrier and $L_{GB} = 350$ Å is the thickness of the graded barrier. Therefore, the ratio of the short wavelength gain at high and low temperatures is expected to be $g_{SW,HT}/g_{SW,LT} = F_{MB,HT}/F_{MB,LT} = 2.75$. This ratio is in good agreement with the observed factor of three enhancement of $g_{SW,HT}$ over $g_{SW,LT}$. Therefore, nonlinear voltage drop within each MQW period is a possible explanation for the enhancement of the short wavelength gain peak at negative voltages above $T = 50$ K.

7. Conclusions

In conclusion, we have investigated the temperature dependence of photoresponse of electron transfer based voltage tunable two-color QWIPs. For $T \leqslant 40$ K, the responsivity peak switches from

7.2 μm under positive bias to 8.6 μm at large negative bias. At higher temperatures, the short wavelength peak is present for both bias polarities and increases rapidly with temperature. In order to investigate this temperature dependence, we extracted the spectra of absorption coefficient and photoconductive gain at different temperatures using CQWIPs with different corrugation periods. We determined the LQW and RQW populations from the deduced absorption spectra and found that, for $T \geqslant 50$ K, the LQW population increases at low negative bias but decreases at high negative bias. The deduced gain spectra indicated a strong enhancement of the short wavelength gain and a strong reduction of the long wavelength gain for $T \geqslant 50$ K. We argued that both these temperature dependences are caused by the large thermal currents from the LQW, which has a significantly lower activation energy than the RQW.

The present detector design requires only one indium bump contact for each pixel of a focal plane array instead of three indium bump contacts in the usual two-color camera design [5,6]. This simplification will greatly facilitate the production of QWIP cameras and increase the yield. On the other hand, due to ineffective electron transfer at high temperatures, the detector needs to be operated below its wavelength switching temperature of 40 K, which is approximately 20 K below the background limited temperature of one-color detectors with similar cutoff wavelengths [1]. One might be able to push the maximum operating temperature up by going to shorter detection wavelengths. Shorter wavelengths would require higher AlGaAs barriers that would lower thermal currents. However, at shorter wavelengths, the photoexcited state is close to the L-valleys in the AlGaAs barriers, which would presumably lower the photoconductive gain. Therefore, more work is required to determine an optimized two-color structure that would yield the highest possible operating temperature.

Acknowledgements

The work at Princeton University is supported by grants from the Army Research Office and the National Science Foundation. Sandia is a multiprogram laboratory operated by Sandia Corporation, a Lockheed Martin Company, for the United States Department of Energy under contract no. DE-AC04-94AL85000.

References

[1] K.K. Choi, The Physics of Quantum Well Infrared Photodetectors, World Scientific, River Edge, New Jersey, 1997.
[2] S.D. Gunapala, H.C. Liu, H. Schneider (Eds.), QWIP 2000, Elsevier, New York, 2001.
[3] A. Kock, E. Gornik, G. Abstreiter, G. Bohm, M. Walther, G. Weimann, Appl. Phys. Lett. 60 (1992) 2011.
[4] M.Z. Tidrow, J.C. Chiang, S.S. Li, K. Bacher, Appl. Phys. Lett. 70 (1997) 859.
[5] S.D. Gunapala, S.V. Bandara, A. Singh, J.K. Liu, S.B. Rafol, E.M. Luong, J.M. Mumolo, N.Q. Tran, D.Z.Y. Ting, J.D. Vincent, C.A. Shott, J. Long, P.D. LeVan, IEEE Trans. Electron Dev. 47 (2000) 963.
[6] M. Sundaram, S.C. Wang, M.F. Taylor, A. Reisinger, G.L. Milne, K.B. Reiff, R.E. Rose, R.R. Martin, Infrared Phys. Technol. 42 (2001) 301.
[7] K.K. Choi, B.F. Levine, C.G. Bethea, J. Walker, R.J. Malik, Phys. Rev. B 39 (1989) 8029.
[8] S.R. Parihar, S.A. Lyon, M. Santos, M. Shayegan, Appl. Phys. Lett. 55 (1989) 2417.
[9] Y.J. Mii, R.P.G. Karunasiri, K.L. Wang, M. Chen, P.F. Yuh, Appl. Phys. Lett. 56 (1990) 1986.
[10] B.F. Levine, C.G. Bethea, V.O. Shen, R.J. Malik, Appl. Phys. Lett. 57 (1990) 383.
[11] K. Kheng, M. Ramsteiner, H. Schneider, J.D. Ralston, F. Fuchs, P. Koidl, Appl. Phys. Lett. 61 (1992) 666.
[12] Y.H. Wang, S.S. Li, P. Ho, Appl. Phys. Lett. 62 (1993) 93.
[13] K.K. Choi, B.F. Levine, C.G. Bethea, J. Walker, R.J. Malik, Appl. Phys. Lett. 52 (1988) 1979.
[14] H.C. Liu, M. Buchanan, Z.R. Wasilewski, J. Appl. Phys. 68 (1990) 3780.
[15] N. Vodjdani, B. Vinter, V. Berger, E. Bockenhoff, E. Costard, Appl. Phys. Lett. 59 (1991) 555.
[16] H.C. Liu, A.G. Steele, M. Buchanan, Z.R. Wasilewski, J. Appl. Phys. 70 (1991) 7560.
[17] V. Berger, N. Vodjdani, P. Bois, B. Vinter, S. Delaitre, Appl. Phys. Lett. 61 (1992) 1898.
[18] A. Majumdar, K.K. Choi, L.P. Rokhinson, D.C. Tsui, Appl. Phys. Lett. 80 (2002) 538.
[19] A. Majumdar, K.K. Choi, L.P. Rokhinson, J.L. Reno, D.C. Tsui, J. Appl. Phys. 91 (2002) 4623.
[20] A. Majumdar, K.K. Choi, J.L. Reno, L.P. Rokhinson, D.C. Tsui, Appl. Phys. Lett. 80 (2002) 707.
[21] C.J. Chen, K.K. Choi, M.Z. Tidrow, D.C. Tsui, Appl. Phys. Lett. 68 (1996) 1446.
[22] C.J. Chen, K.K. Choi, L. Rokhinson, W.H. Chang, D.C. Tsui, Appl. Phys. Lett. 75 (1999) 3210.

[23] K.K. Choi, C.J. Chen, D.C. Tsui, J. Appl. Phys. 88 (2000) 1612.
[24] K.W. Goossen, S.A. Lyon, K. Alavi, Appl. Phys. Lett. 52 (1988) 1701.
[25] L.J. Kozlowski, G.M. Williams, G.J. Sullivan, C.W. Farley, R.J. Anderson, J. Chen, A.T. Cheung, W.E. Tennant, R.E. DeWames, IEEE Trans. Electron Dev. 38 (1991) 1124.
[26] E. Pelve, F. Beltram, C.G. Bethea, B.F. Levine, V.O. Shen, S.J. Hsieh, R.R. Abbott, J. Appl. Phys. 66 (1989) 5656.
[27] B.F. Levine, C.G. Bethea, G. Hasnain, V.O. Shen, E. Pelve, R.R. Abbott, S.J. Hsieh, Appl. Phys. Lett. 56 (1990) 851.
[28] B.F. Levine, A. Zussman, J.M. Kuo, J. de Jong, J. Appl. Phys. 71 (1992) 5130.